JOURNAL OF CATALYSIS **169,** 455–468 (1997)
ARTICLE NO. CA971701

Identification of Coke Precursors in Heptane Reforming with a Multioutlet Fixed-Bed Reactor and a Novel Vibrational Microbalance

K. Liu,*,†,[1] S. C. Fung,† T. C. Ho,† and D. S. Rumschitzki*,[2]

*Department of Chemical Engineering, City College of City University of New York, New York, New York 10031; and †Corporate Research Laboratories, Exxon Research and Engineering Company, Annandale, New Jersey 08801

Received November 4, 1996; revised March 19, 1997; accepted March 20, 1997

This work aims to determine the major coke precursors in *n*-heptane reforming over a commercial Pt–Re/Al_2O_3 catalyst. We employ both a multioutlet fixed-bed reactor and a new microbalance that measures coke-on-catalyst by monitoring the natural vibrational frequency of a tapered element that is pinned at one end and has catalyst at its free end. This microbalance does not have the gas bypass problem common to conventional gravimetric microbalances. We show that five-carbon ringed naphthenes (C5N) are the only reforming reaction participant species lump whose concentration rises whenever the rate of catalyst activity loss increases in response to changes in temperature, pressure, or space velocity. A more quantitative treatment shows that the C5N concentration profile along the fixed-bed reactor tracks both the coke profile and the profile of a measure of the local catalyst deactivation rate. Further detailed microbalance studies with different hydrocarbon feeds show that the coking rate is first order in C5N and is almost independent of toluene concentration. The C5N formed in *n*-heptane reforming quantitatively accounts for most of the coke produced. All experiments pointed to C5N as the major coke precursor in *n*-heptane reforming.

INTRODUCTION

Catalyst deactivation by coke deposition is ubiquitous in catalytic hydrocarbon processing. To improve and develop more robust catalysts, one has to understand the mechanism and kinetics of the coking reactions. Although there have been numerous studies on the deactivation of bifunctional reforming catalysts by coke deposition, the interpretations of the results sometimes diverge. Butt and Petersen (1) and Franck and Martino (2) review this field thoroughly.

Attempts to model the coking processes of catalysts (3–5) have gleaned some insight into the kinetics; however, these studies have not provided a complete understanding of the origin, the nature, or the location of the coke deposited. Furthermore, most coking kinetics models thus far are in Voorhies' form, the power law correlation of the amount of coke with time on-stream (6). Relatively few coking kinetics studies correlate the coking rate with the actual coking reaction conditions, such as the partial pressures of hydrogen and of the hydrocarbon, the amount of coke on the catalyst, and the operating temperature. Such a study is difficult to carry out; after all, coke represents only a few parts per million of the reaction products under realistic reforming conditions (2) and coking experiments require as long as hundreds of hours. The literature contains several coke buildup mechanisms (7–9). They all involve an initial step of dehydrogenation and the formation of unsaturated species on metal sites. These unsaturated species are then able to migrate, either via the gaseous phase or through the adsorbed phase, to the acid sites of the catalyst where they form dimeric or polymeric species.

The purpose of the present work is to gain a better quantitative understanding of the processes of coke formation in *n*-heptane reforming over an unsulfided supported Pt–Re catalyst and of their kinetics. We choose the reforming of *n*-heptane as a representative model system for commercial reforming. It falls within the C_6–C_9 range of typical reformer feeds and its reactions are representative of those of C_8 and C_9 paraffins (10, 11). The heavier normal paraffins are expensive to obtain at high enough purity for analytical work, and the analysis of their reaction products is quite complex. Accordingly, the kinetic analysis of *n*-hexane reforming would seem to be the simplest choice. Hexane's reactions, however, are not representative of C_7–C_9; it reacts primarily to form isohexanes with a poor selectivity to aromatics compared with C_7–C_9 paraffins.

There are more than 60 hydrocarbon compounds formed in *n*-heptane reforming, as gas chromatography (GC) analysis indicates. Theoretically, all of these compounds contribute to some degree to the deactivation of a catalyst by coke deposition. There are some indications that naphthenes with five-carbon rings are among the most potent coke precursors (7, 12, 13); however, conclusive

[1] Current address: Mobil Technology Company, Paulsboro, NJ 08066.
[2] To whom correspondence should be addressed.

0021-9517/97 $25.00

experimental proof as to which is the major coke precursor is not yet available, and the literature contains differing conclusions. Therefore, the first step in a fundamental look at catalyst coking is the determination of the precursor species, from among the catalytic reaction participants, that go on to form coke. Aside from its fundamental value for the understanding of the coking process, knowledge of the major coke precursor would have an important practical impact. Since it is very difficult to monitor the coke formation *in situ* in a commercial reformer, but it is easier to monitor the gas-phase composition along the catalyst bed, one might ask: Is it possible to calculate the coke amount at any time and position along the catalyst bed simply by monitoring the gas-phase coke precursor concentration as a function of position and time on-stream? A positive answer would require a knowledge not only of what the major coke precursor is but also of how and with what kinetics it produces coke. That is, after identifying the major precursor, one can run experiments with it to focus on the reactions from precursor to coke. The present work presents a detailed determination of the major coke precursor and a very simple kinetic model for correlating the deactivation data. It also clarifies certain ambiguities and controversies in earlier work.

To carry out the work we have at our disposal an integral fixed-bed reactor with four outlets along the catalyst bed from which we can continuously monitor gas-phase composition. It is similar to the one Marin and Froment (14) used earlier. This multioutlet reactor also allows us to measure the coke profile along the catalyst bed. A temperature-programmed oxidation (TPO) apparatus provides a detailed analysis and classification of the coke on the catalyst particles discharged from each of the individual sections. Unfortunately, each coking data point obtained this way comes at the end of a run. Thus a large number of long-time runs are needed to procure meaningful data for coking kinetics studies. In light of this, we have also developed a novel, flow-through, vibrational microbalance reactor that is capable of *in situ*, simultaneous measurement of coke buildup and gas-phase composition.

This paper begins by describing the experimental apparatus and operating parameters. Following this is a summary of some general trends regarding the effects of process variables on catalyst coking and on the concentrations of various reforming intermediates. Here one notes a definite correlation between the coke formation and the concentration of C5 naphthenes (C5N) present under those conditions. We then embark on a kinetic analysis that tracks the profiles of the coke amount, the C5N concentration, and the catalyst activity, all as functions of position along the fixed-bed reactor. Finally, we present microbalance data, which, together with the previous data, constitute a package of very strong and varied evidence that C5Ns are the major coke precursors.

EXPERIMENTAL

Activity Tests in the Multioutlet Fixed-Bed Reactor

The reactor is fabricated from a 1.27-cm-o.d. stainless-steel tube with an i.d. of 1.02 cm. Reference (13) details the setup and operation of the multioutlet rector. It has four outlets along its wall, which permit sampling of the gas at four bed heights, corresponding to four different space times for a given flow rate and catalyst packing. A computer-controlled stream selection valve automatically connects one of the outlets to the GC sample coil. A needle valve upstream of the stream selection valve drops the pressure of the outlet stream to atmospheric pressure and controls its flow rate to the GC sample coil. Heat tracing of the sample stream flow path to 483–543 K ensures that the total product is in the vapor phase. Since the sample stream extracts less than 5% of the total volumetric flow traversing the catalyst bed, there is little change in the space velocity due to the diversion of the sample stream.

A three-zone furnace with independent PC-programmed temperature controllers provides varying heat input to different sections of the reactor to facilitate isothermal operation. Also, dilution of the catalyst (1.6-mm extrudates) with inert randomly shaped quartz particles with an average diameter of 1.0 mm is necessary to avoid axial temperature gradients that would otherwise result from the highly endothermic character of the aromatization reaction. These measures give essentially a uniform temperature profile along the 33-cm reactor. The Thiele modulus (based on a molecular diffusivity of 0.74 cm^2/sec and a Knudsen diffusivity of 0.14 cm^2/sec for heptane in hydrogen at 772 K, Bousanguet's additive resistance law and a factor of 1/10 to account for diffusion in tortuous pores, and an average pore diameter of 105 Å) of 0.7 for the reactor runs, for first-order reactions and rate constants typical of the system at hand, gives an effectiveness factor of 0.9. Although we could have used smaller particles and obtained a higher effectiveness factor, our interest was to employ the most widely used industrial catalyst, the 1.6-mm extrudates.

A typical run's loading consists of a total of 5 g of catalyst, diluted with quartz particles of a fairly uniform size, in the four catalyst sections above outlet 4. Table 1 shows the different loadings of the catalyst in the reactor's four sections and the corresponding space velocities. The catalyst loading above the ith outlet is labeled section i ($i = 1, \ldots, 4$). A half-inch section of quartz particles separates the sections from each other to avoid ambiguity in the amount of catalyst attributed to each section. We vary the conversion either by changing the feed rate for a given catalyst loading distribution or by changing the catalyst loading of different sections for a given overall feed rate. The reforming conditions for *n*-heptane on the Pt–Re/Al_2O_3 catalyst are similar to those in commercial units. Specifically, temperatures are 733, 750, 772, 783, and 794 K at 517 kPa. At each

TABLE 1

Catalyst Loading and Corresponding Space Velocities of Different Sections

	Run 1				Run 2				Run 3			
Outlet number	4	3	2	1	4	3	2	1	4	3	2	1
WHSV (g/hr-g cat.)	2	4	10	110	6	14	26	120	8	18	57	133
Catalyst loading (g)	2.5	1.5	0.91	0.09	2.85	1.0	0.9	0.25	2.8	1.5	0.4	0.3

temperature, three runs totaling 12 liquid weight hourly space velocities (WHSVs) constitute the kinetic data. Experiments at 207, 345, 517, and 1034 kPa at 750 K provide the total pressure dependence of the kinetics. To keep the number of manipulated variables small, we fix the hydrogen-to-hydrocarbon mole ratio in all experiments at 3, a value typical of commercial operation.

The procedures used for catalyst pretreatment appear in detail in (13) and a summary follows: After loading, heating the catalyst from room temperature to 789 K at 3 K/min under 2000 cm^3/min (at ambient conditions) of hydrogen and maintaining this temperature for 8 hr reduces the catalyst *in situ*. A gradual, 3-hr cooling of the reactor to 643 K precedes the introduction of the *n*-heptane reactor feed. A subsequent slow, 3-hr heating of the reactor brings it to run temperature. On-stream time begins the moment the reactor attains a preselected temperature. A stream selection valve directs the reaction products from each of the outlets to an HP5880 gas chromatograph equipped with a 50-m capillary column coated with crosslinked methylsilicone gum. The lip of each outlet port extends approximately 1 mm (about one particle diameter or one-fifth of the tube radius) into the reactor, thereby ensuring that the withdrawn stream is not a wall artifact.

At the end of the run the liquid feed is stopped and the reactor is cooled to 643 K over 3 hr and maintained at this temperature for 5 hr in hydrogen flowing at 430 cm^3/min. This procedure strips the reversibly adsorbed hydrocarbons off the catalyst, so as not to contribute to the TPO signal during the analysis of the catalyst coke. Following the 643 K hydrogen stripping, the reactor is cooled to room temperature under flowing hydrogen.

After the termination of the run, one discharges the catalyst in discrete sections without mixing so as to be able to compare the coke content of each section with the activity measurements.

Coking in a Flow-Through Vibrational Microbalance

Conventional thermogravimetric analyzer (TGA) microbalances have long played an important role in catalyst coking and decoking kinetics studies (15–18); however, these TGA microbalances have a number of limitations. First, since a large but unmeasurable portion of the feed gases bypasses the catalyst bed, one can determine neither the true space velocity nor the actual reaction conditions that the catalyst bed experiences. Thus the intrinsic reaction kinetics remain inaccessible due to these poorly defined conditions. This is true even when one conducts the reaction at low conversions because dilution by the bypassed feed gas can give a low apparent conversion at the TGA exit, while the actual conversion across the catalyst basket is high. Second, TGAs can suffer external diffusion limitation. Thin layers (one to two particles deep) of catalyst particles (18) and high flow rates can minimize such problems, but the necessarily large particle sizes, say, in the range of 0.07–0.1 cm (the flow in the TGA can blow finer particles out of the basket), are likely to encounter internal diffusion limitations for fast reactions. Finally, TGA microbalances are not accurate for small weight changes below 1% because of significant buoyancy and drag effects when one switches from carrier gas to feed gases (18).

To overcome these difficulties we have developed a novel inertial microbalance system for high-temperature and moderate-pressure operation at both high and low conversions. Reference (19) gives a preliminary description of this equipment. We now expand on this preliminary report and tie it to the application of coking in the *n*-heptane reforming system. The major advantage of the new design is that it provides a packed bed of catalyst through which all the feed gases flow. It detects changes in the catalyst mass located at the tip of a tapered element by sensing the changes in its vibrational frequency. Because of its inertial design, it can enclose a packed bed of catalyst through which feed vapor flows at considerable rates, without significant flow-induced buoyancy and drag effects. This design can measure transient mass gains and losses with a 0.1-sec time resolution, permitting the observation of transient adsorption and desorption and coking and decoking kinetics under realistic conditions.

Patashnick *et al.* (20) first reported this TEOM microbalance as a device to quantify dust particles suspended in air at ambient condition. Recently, Hershkowitz *et al.* (21) reported a pulse adsorption study of hydrocarbons on Y-zeolite using an R&P (Rupprecht and Patashnick Co., Albany, NY) vibrational microbalance. R&P custom-manufactured our microbalance, a high-temperature, moderate-pressure, gram-size-catalyst-loading, highly stable vibrational microbalance for long-term catalyst deactivation studies under plug-flow conditions. It led to R&P's

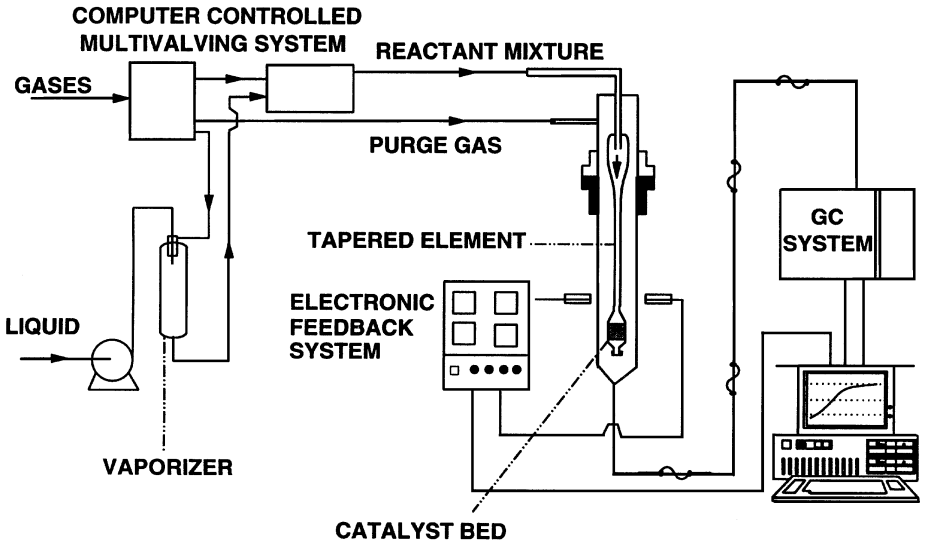

FIG. 1. Flow diagram of the flow-through, vibrational microbalance.

subsequent development of the Model 1500 Pulse Mass Analyzer, which, as in our system, uses mechanical energy and an optical feedback device to oscillate the tapered element at its natural frequency.

Let us expand on our earlier brief description (19) of the vibrational microbalance reactor system. It consists of a flow-through tapered element oscillating microbalance, a valving control feeding unit, and a product analysis unit. Figure 1 shows the diagram of this unit. It can operate at up to 923 K and 514 kPa. The control unit contains the support hardware necessary to perform, record, and display real-time measurements with the microbalance optical sensor unit, including temperature and pressure controllers and feedback circuitry to maintain the oscillation of the tapered element. The product analysis unit contains an HP 5890 gas chromatograph and a computer with Chrom Perfect software for collecting and processing the gas chromatograph data. Since the tapered element has to vibrate freely, it is not possible to connect the sample cell outlet directly to the gas chromatograph for analysis. Therefore, a stainless-steel tube houses the tapered element and the system requires an inert gas (He) to purge the space between this outer tube and the tapered element (Fig. 1) so that the downstream gas chromatograph samples the true instantaneous change in gas composition.

The microbalance itself is made up of a hollow tapered tube with a material test bed located at its tip. Catalyst particles, held in place by packed quartz wool and an end cap, fill the material test bed. The other end of the tapered element is fixed. As the carrier or sample gas flows through the tapered element and the catalyst bed, the system records changes in the mass of the catalyst as a result of interactions with the gas stream.

An electronic feedback system maintains the oscillation of the tapered element with the catalyst bed on its end in a clamp-free mode. A feedback circuit uses mechanical energy to drive the tapered glass element to its natural frequency oscillation. The materials and mountings have very small losses and result in an oscillating system with very low damping. Such systems oscillate very easily and are sharply tuned at their resonant frequencies. This natural frequency is a function of the mechanical properties of the glass, as well as the inertia of the glass and catalyst bed. As this inertia changes, so does the natural frequency. The microbalance detects changes in the mass m of the catalyst by monitoring frequency ν changes and using the cantilever beam, mass-spring equation $\nu(m) = (\kappa/m)^{1/2}$, where ν is the natural frequency of the spring-mass system, κ is the spring (tapered element) constant, and m is the total oscillating mass (catalyst bed mass + mass deposited or lost + part of the tapered element mass).

To determine the spring constant κ, one adds a known weight to the sample cell, such as the cap. If κ does not change as the mass in the sample cell changes, then $\kappa = \Delta m\{[\nu^2(m + \Delta m)]^{-1} - [\nu^2(m)]^{-1}\}^{-1}$. To decrease the noise and improve the detection limit of the measurements, the catalyst particles are tightly packed in the sample cell to ensure no movement of the catalyst particles as the tapered element vibrates. We have on many occasions repeated experiments with fresh catalysts and found that the data varied by less than 10% between experiments. The stability of the balance is excellent. It drifts less than 0.1 wt% in 60 hr. This facilitates long-term coking measurements. The sensitivity of the balance depends on the catalyst loading. We have designed two tapered elements with sample cells to hold about 0.1 and 1 g of catalyst particles

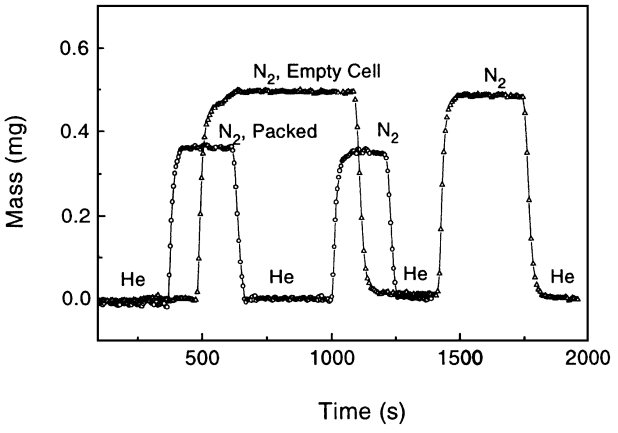

FIG. 2. Accurate and reproducible detection of the tiny mass change resulting from switching the carrier gas from He to N_2 in the empty 0.1-g cell and in the cell packed with quartz particles.

for this microbalance. For a vibrating element assembly designed to hold 0.1 g catalyst, it detects a mass change of $\sim 5\ \mu$g.

Due to the high sensitivity of this balance, the mass of the gases occupying the "void space" in the catalyst bed (including the internal pores of the catalyst particles) and, to a much lesser extent due to the shorter distance to the pinned end, the void space in the rest of the hollow tapered element, both affect the vibrational frequency of the balance. On switching carrier gases, the microbalance can detect changes in mass due to the density difference of the two gases, even when no adsorption or coking occurs. Figure 2 demonstrates this sensitivity and reproducibility for a switch from He to N_2 at 300 cm^3/min and ambient conditions in the empty 0.1-g taper element. Therefore, one needs to know what fraction of the total cell mass is due to the gas itself; i.e., one has to measure the "effective volume" (total void space in the tapered element including the sample cell and the flow path from the pinned end to the sample cell) in each experiment to be able to take this effect into account when switching from an inert gas to a feed gas or when adding a feed gas to a hydrogen stream. Generally, the mass change due to gas density change has a minor influence on the measurement of coking kinetics, mostly during the initial coking period; however, it becomes very important when one wants to measure adsorption and desorption rates. It is easy to account for this gas density change once the "effective void volume" is known.

To measure this "effective volume," one introduces a step change in the gas density in the tapered element by, for example, switching from one inert gas to another, e.g., from helium to nitrogen and vice versa, while maintaining the same purge gas. This generates a change Δm in the measured mass from which one can calculate the "effective volume" V_g from the ideal gas law: $V_g = \Delta m RT/[(M_2 - M_1)P]$. Here M_2 and M_1 are the molecular weights of the inert gases that generate a change Δm in the measured mass, P is the pressure, T the temperature, and R the ideal gas law constant. One determines the actual adsorption plus coke deposition amount on the catalyst by subtracting the mass change due to the gas density difference from the measured value. Figure 2 shows the microbalance-measured results of switching the carrier gas from He to N_2 in the empty 0.1-g cell and the cell packed with 60/80-mesh quartz particles, respectively. With the measured results, one can determine the volume of the empty cell as well as the volume of the quartz particles and the porosity of the bed. Thus, with this vibrational microbalance, one not only can measure the coke amount but also can determine the catalyst's pore volume change due to coke deposition by flowing two different inert carrier gases through the fresh and heavily coked catalyst bed, respectively. From these data, one can attempt to ascribe the deactivation to site coverage or to pore blockage. This is another important feature of the novel vibrational microbalance.

Coke Analyses

We measured the weight percentage of coke in each catalyst section of the fixed-bed reactor by a highly sensitive temperature-programmed oxidation technique, using a modified Altamira temperature-programmed unit (Model AMI-1). A Ru catalyst converts the CO_2 produced during coke oxidation to methane that a flame ionization detector continuously monitors. TPO analyses use a 1% O_2 in He mixture flowing at 60 cm^3/min through the sample while increasing the temperature at a rate of 13 K/min from room temperature to 1043 K. Sample weights were about 20 mg. Reference (22) describes the details of these analyses.

Materials

The gases used in this research are cylinder hydrogen of electrolytic grade (99.95%), cylinder helium (99.95%), and cylinder nitrogen (99.95%). The liquid feed *n*-heptane (nC_7), methylcyclopentane (MCP), ethylcyclopentane (ECP), and 2-methylhexane (2MH) are all analytical pure grade (99 mol%). The bimetallic Pt–Re/Al_2O_3 catalyst, in the form of 1/16-in. extrudate, contains 0.3 wt% Pt, 0.3% Re, and 0.9 wt% Cl, and has a BET specific surface area of 200 m^2/g. We neither presulfide the catalyst nor add sulfur to the feed during the run. Catalyst particle sizes are 177–250 μm (60/80 mesh) in the microbalance experiments.

RESULTS OF FIXED-BED EXPERIMENTS

Comparison between the Microbalance and the Fixed-Bed Reactor

Recall that the reaction mixture's space velocity and composition in the catalyst bed are inaccessible in a conventional thermogravimetric microbalance, since a

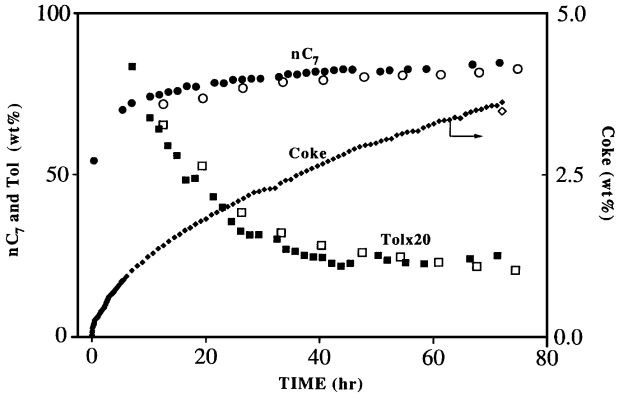

FIG. 3. Comparison of the data obtained from the vibrational microbalance (filled symbols) and the fixed bed (open symbols).

large but unmeasurable portion of the feed gas bypasses the catalyst bed. To demonstrate that the vibrational microbalance overcomes this problem, we have carried out experiments in both the microbalance and the multioutlet fixed-bed reactor with the $Pt–Re/Al_2O_3$ catalyst under the same conditions: 210 kPa, 750 K, $H_2/nC_7 = 3$, and 28 WHSV. As discussed, diffusion effects are quite small in the reactor and negligible in the microbalance due to the much smaller catalyst particles.

Figure 3 compares nC_7 and toluene concentrations exiting the two reactors as functions of on-oil time. Within experimental error, toluene yields and unconverted nC_7 fractions for both units are virtually the same during the entire 80-hr run. These results point to the importance of reliably measuring the space velocity in the microbalance reactor.

Another point of note is that, in contrast to TGA microbalances (18), the present vibrational microbalance even provides initial coking rate data (see Fig. 3), since the mass corrections due to gas density change on introduction of the nC_7 feed are easy to make. Coke deposition is initially very fast, and slows as the catalyst deactivates. For the fast coking processes such as catalytic cracking, the catalyst gets coked in a few seconds; thus, there is an obvious advantage in being able to observe this fast coking regime directly.

The foregoing results show that the present microbalance reactor not only permits *in situ* coking kinetics measurements, but also gives reliable catalyst activity and selectivity data from which one can determine the kinetics of the main reactions. Before discussing the data obtained from the vibrational microbalance, let us look at some general trends observed from the integral fixed-bed reactor.

Deactivation in the Multioutlet Reactor: Effects of Process Variables

Effect of pressure. In this series of experiments we vary the total pressure while holding the H_2/nC_7 ratio and other conditions constant. Figure 4 plots nC_7 conversion at outlet 4 (reactor exit) versus on-stream time for different pressures at 750 K. As the pressure increases, the conversion of nC_7 also increases. At a low pressure of 207 kPa the catalyst deactivates rapidly, and the conversion of nC_7 drops from 80% (weight basis) initially to 40% after about 120 hr. At higher pressures nC_7 conversion level is relatively flat with on-stream time. GC analysis of the nC_7 reforming product stream yields about 60 peaks. For C5N, there are a total of 4 major peaks (1,2- and 1,3-dimethylcyclopentane, methyl- and ethylcyclopentane). The other major peaks include two isoheptanes (2- and 3-methylhexane), aromatics (benzene, toluene, and xylenes), cracking products (C_i, $i = 1, \ldots, 6$), and unreacted *n*-heptane. All other peaks are minor. We examined each of these major species individually as well as summing both major and mirror peaks into the lumps C5N, $C_6–$, aromatics, and isoheptanes (iC_7). Although not shown, plots for iC_7, toluene, and cracked products show that at 207 kPa the toluene yield begins as high as 27% and drops to 7%. After the initial transient catalyst deactivation period, the higher the pressure, the more toluene the reaction produces. Higher operation pressures also lead to more cracking products. For instance, after 80 hr on-stream, the yield of cracking products increases from 10% at 207 kPa to 32% at 1034 kPa. On the other hand, iC_7 seems to go through a maximum of 37% with respect to pressure near 517 kPa.

Figure 5 shows that the reaction produces more C5N at lower pressures. For instance, after 80 hr on-stream, the total C5N concentration at 750 K increases from 1.2% at 1034 kPa to 5.8% at 207 kPa. One also sees that C5N concentration increases as the catalyst deactivates. Note that C5N is the only one of the lumped species whose concentration increases monotonically with decreasing pressure, suggesting that the more C5N produced may correlate with the faster rate of deactivation.

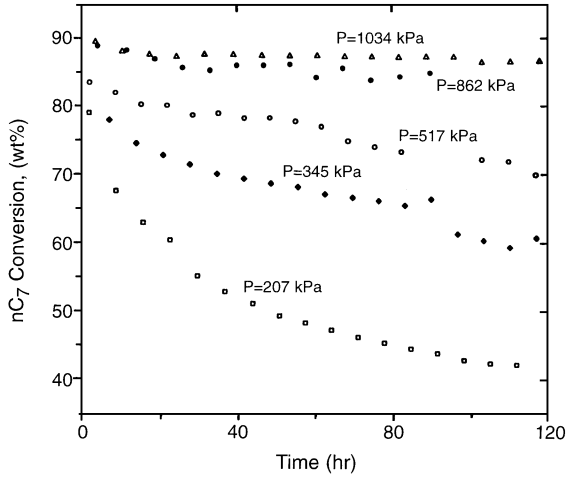

FIG. 4. Effect of pressure on catalyst deactivation, $T = 750$ K.

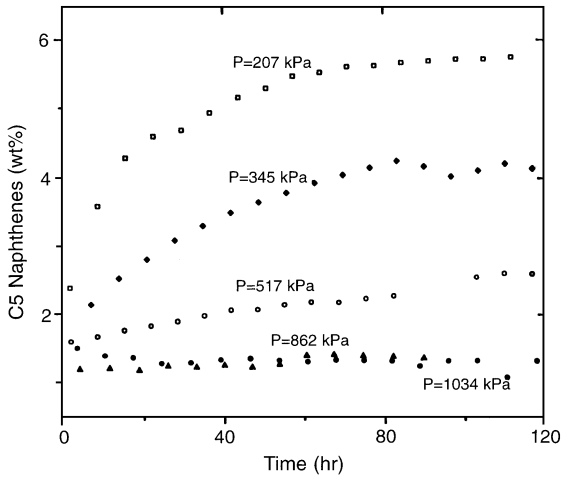

FIG. 5. C5 naphthene concentration as a function of time on-stream at different pressures, $T = 750$ K.

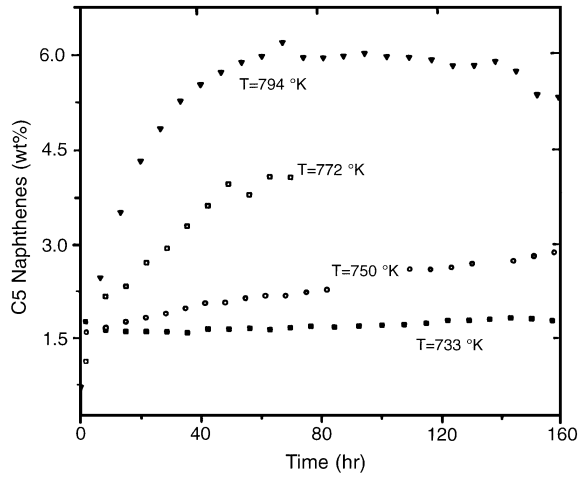

FIG. 7. C5 naphthene concentration as a function of time on-stream at different temperatures, $P = 517$ kPa.

Effect of temperature. Figure 6 shows that the higher the temperature, the higher the initial conversion of nC_7 but the faster the deactivation rate. At 794 K, the conversion of nC_7 at 517 kPa drops from 98% initially to 50% at 160 hr on-oil, whereas at 733 K the conversion is relatively stable between 75 and 68% over the same period. Thus, curves of different temperatures can cross. High temperatures also yield more C_1–C_6 cracking products initially (data not shown); for example, at 794 K the cracking products concentration drops from 36% initially to 18% after 160 hr on-oil, while at 733 K the yield of cracking products (13%) declines slightly over the same period. This behavior mirrors that of nC_7 conversion. On the other hand, the production of iC_7 decreases with increasing temperature. The yield of iC_7 decreased from 40% at 733 K to 11% at 794 K (data not shown). This might be due to a larger amount of iC_7 being cracked at higher temperatures. Finally, Fig. 7 shows that C5 naphthene yield is an increasing function of temperature, e.g., from 1.5% at 733 K to 6.0% at 794 K. This suggests that the faster rate of deactivation at higher temperatures again seems to correlate with the increase in C5 naphthenes at higher temperatures.

Effects of space velocity. Figure 8 is a parametric plot of the effect of space velocity on nC_7 conversion at 773 K, 517 kPa, and $H_2/HC = 3$. The data labeled "outlet 1" correspond to a high equivalent space velocity of 133 w/w/h. The corresponding space velocities for outlets 2, 3, and 4 are 57, 18, and 8 w/w/h, respectively (see Table 1). The nC_7 conversion increases from outlet 1 to outlet 4 at all times and it decreases with on-stream time at each outlet. More relevant here, the rate of deactivation increases as WHSV decreases in the range of high WHSV until a maximum deactivation rate (at outlet 3) is reached. The C5N profiles in Fig. 9 show a similar trend. We shall use the data obtained at different WHSVs below to develop a simple deactivation model that correlates with the extent of local coking in the reactor.

Summarizing, the pressure, temperature, and space velocity trends all show a qualitative correlation between C5N

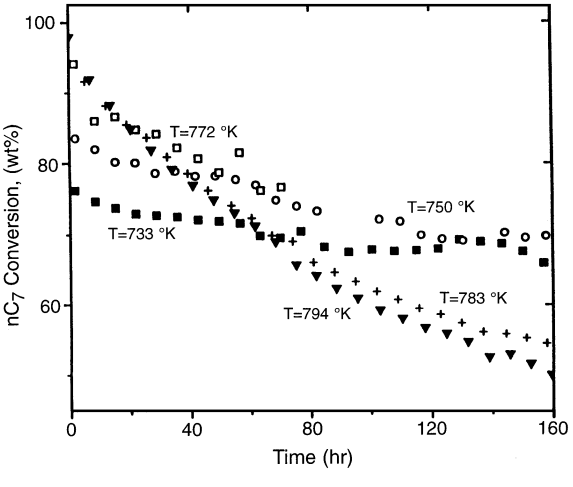

FIG. 6. Effect of temperature on catalyst deactivation, $P = 517$ kPa.

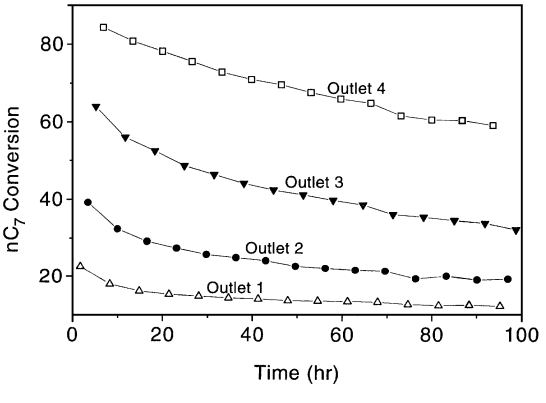

FIG. 8. Conversion of *n*-heptane versus time on-stream at different outlets of the fixed-bed reactor.

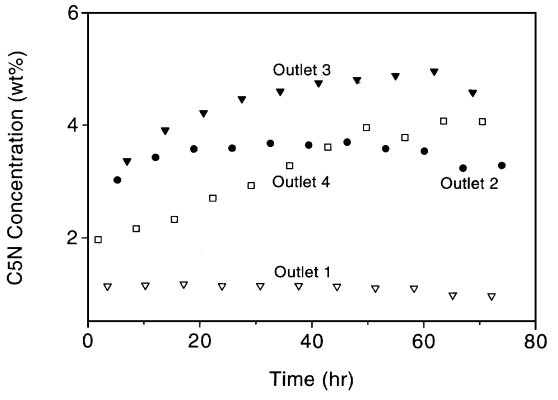

FIG. 9. Total concentration of five-carbon ringed naphthenes versus time on-stream at different outlets of the fixed-bed reactor.

concentration and the rate of catalyst deactivation which is consistent with but does not yet prove the hypothesis that C5N is a potent and major coke precursor. Querini and Fung (13, 23) inferred this connection from some preliminary data. We now proceed to a quantitative treatment.

MODELING OF CATALYST DEACTIVATION

The goal of this work is to identify the principal reforming reaction participant(s) responsible for leading to the decrease in catalyst performance with on-oil time. It is common to think of this quest interchangeably with the search for the major coke precursors(s). This begs the question of the relationship between catalyst activity and coke content, which is usually purely empirical.

One approach to these issues that is appropriate to the type of data accessible to the multioutlet fixed-bed reactor is to find, if possible, an appropriate measure of the catalyst activity based solely on gas-phase concentrations, and to examine how this activity decays with time at each space velocity. Clearly this latter measure should depend on the concentration of the as yet unknown precursor. Next, one simultaneously plots this activity-decay measure, the local rate of coke formation and the concentrations of the candidate culprits versus space time. Such a plot can verify if there is indeed a unique relationship between activity and coke amount and, of more immediate relevance, can differentiate between those gas-phase species that are likely to be major coke precursors and those that are not.

There is a well-established technique for extracting an activity-decay measure from conversion versus on-stream time and space time that dates back to Szepe and Levenspiel (24). This treatment presumes that a reaction involving α surface sites and the main reactant, *n*-heptane in the present discussion, depletes this reactant's concentration and exclusively accounts for its time evolution. It is, however, well known [e.g., (10, 25)] that *n*-heptane undergoes a fast, reversible reaction with a collection of isoheptanes (iC_7), which we may lump into the pseudospecies C. Thus, below we extend Szepe and Levenspiel's analysis to include a reversible reaction between the main reactant A and species C. That is, we deal with a lumped reaction scheme of the form $C \leftrightarrow A \rightarrow B$, where B is the lump of all hydrocarbon products other than iC_7. With this simple reaction scheme, we wish to find an approximate measure of local catalyst decay rate based on the on-stream behavior of A and C. We shall show that, under a set of assumptions that are appropriate and many of which are experimentally verifiable, the final results reduce to tractable expressions.

Since the catalyst deactivates, the net consumption rate $-r_A[\mathbf{c}(s,\tau)]$ $(0 \le s \le t)$ of A depends on the current species concentration vector as well as on the concentration history that the catalyst has seen over its on-stream time t at its particular position (space time τ in the reactor). Suppose that the deactivation affects all reactions contributing to r_A similarly and proceeds over a much longer time scale than the main reactions. Suppose also that the catalyst deactivation depends only on the concentration c_p of coke precursors whose local value $c_p(t,\tau) \approx c_p(\tau)$ has not varied much over the catalyst's on-stream time t. For example, Fig. 9 illustrates that after the initial transient, the concentration of C5Ns is usually relatively insensitive to t. Following Szepe and Levenspiel (24), we split r_A into the product of a fresh catalyst rate r_{A0} that depends on the instantaneous local concentration vector $\mathbf{c}(t,\tau)$ and an activity function a that depends in principle on the local concentration history of the catalyst. Accordingly,

$$r_A[\mathbf{c}(s,\tau)] = a[\mathbf{c}(s,\tau)] \cdot r_{A0}[\mathbf{c}(t,\tau)]$$
$$= a(t, c_p^*, \tau) \cdot r_{A0}[\mathbf{c}(t,\tau)], \quad 0 \le s \le t. \quad [1]$$

Suppose the reactions that deplete A are all qth order in c_A and their rate constants sum to k_A. Suppose also that the reaction $C \rightarrow A$ is first order with rate constant k_C. If the rate of change of the concentration of the active sites or the fraction f of the catalyst's unused fouling capacity is nth order in f with rate constant k_d, and if a represents the simultaneous availability of α active sites for the main reactions ($a = f^\alpha$), one can describe the system by the following pseudohomogeneous fixed-bed model:

$$\frac{dc_A}{d\tau} = r_A = a r_{A0} = \left(k_C c_C - k_A c_A^q\right) a,$$
$$c_A = c_{A0} \text{ at } t = 0; \quad [2]$$

$$\frac{df}{dt} = -k_d f^n F(c_p) = -K_d f^n, \quad f = 1 \text{ at } t = 0. \quad [3]$$

Here the deactivation pseudoparameter K_d is the proposed measure of the local rate of catalyst deactivation. Note that $K_d = k_d F(c_p)$ depends on the local concentration of precursor (which depends on τ), but is, by hypothesis, time invariant.

That a is a function of τ through c_p makes it impossible to integrate Eq. [2] explicitly because we do not know the

functional dependence of a on τ; however, assuming that $c_p(\tau)$ and $a(t, c_p)$ are continuous, one can use the mean value theorem to integrate Eq. [2] from ith to the $i+1$st outlet. If $k_C \neq 0$, the integration is straightforward for $q = 0$ and 1. Thus, after some algebra, we have

$$\ln \frac{c_A(\tau_i)}{c_A(\tau_{i+1})} = -\bar{k}_i \langle a \rangle_i (\tau_{i+1} - \tau_i), \quad i = 0, 1, 2, 3 \; (q = 1), \tag{4}$$

$$\bar{k}_i = k_A \left\{ 1 - \frac{\ln\left[1 + \frac{k_c}{c_A(\tau_i)} \int_{\tau_i}^{\tau_{i+1}} \exp\left(k_A \int_{\tau_i}^{\tau} a d\tau'\right) a(\tau) c_c(\tau) d\tau\right]}{k_A \langle a \rangle_i} \right\} \quad (q = 1), \tag{5}$$

$$\langle a \rangle_i = \frac{1}{\tau_{i+1} - \tau_i} \int_{\tau_i}^{\tau_{i+1}} a d\tau, \tag{6}$$

$$c_A(\tau_i) - c_A(\tau_{i+1}) = \bar{k}_i \langle a \rangle_i (\tau_{i+1} - \tau_i), \quad i = 0, 1, 2, 3 \; (q = 0), \tag{7}$$

$$\bar{k}_i = \langle k_c c_c - k_A \rangle_i = \frac{1}{\langle a \rangle_i} \int_{\tau_i}^{\tau_{i+1}} (k_c c_c - k_A) a d\tau \quad (q = 0). \tag{8}$$

Note for $q = 0$, we do not consider the case of reactant exhaustion. Analytic integration for $k_C \neq 0$ and c_C not constant is not easy for other values of q. In Eqs. [5] and [8], $\langle a \rangle_i$ and $\langle k_c c_c - k_A \rangle_i$ are mean values of their arguments between outlets i and $i+1$. According to the integral mean value theorem, between outlets i and $i+1$ there exists at least one point τ_i^*, whose exact position is not specified, at which the activity takes on the value $\langle a \rangle_i$. At τ_i^*, one can substitute the solution of Eq. [3] into Eq. [4] for a to get the forms in Table 2 for various α, n, and q. In the context of the approximations made thus far these forms are exact.

If k_C were zero (no reaction C $\rightarrow$ A) then the $\bar{k}_i$ in Table 2 would simply equal k_A and be independent of τ_i. For $k_c \neq 0$, $\bar{k}_i = \bar{k}_i(\tau_i, \tau_i^*, t)$. Clearly, for $K_{di} = K_d(\tau_i)$ as determined from the multioutlet fixed-bed reactor and one of the correlations in Table 2 to be a useful measure of the local catalyst deactivation rate, $\bar{k}_i$ must be only a very weak function of time t. We shall assume this for the moment and, after determining a set of n and α that is consistent with the data, consider it in detail.

Clem (10) first indicated that, with excess hydrogen, all reactions in n-heptane reforming are first order. In addition, many of the models of n-heptane reforming in the literature (14, 25–27) and the data from which they derive support the choice $q = 1$. For instance, if one uses the Langmuir–Hinshelwood model and the data in these works, one finds that the adsorption term in the denominator is close to unity and varies by less than 5% under the conditions and over the largest difference in space times (0 and 30 min) that we have employed. Moreover, we have done a detailed analysis of n-heptane reforming kinetics over a wide range of conditions and found that (probably for this reason) the reaction network is very well described by first-order kinetics (28). The equilibrium constants derived from the model are consistent with thermodynamic values.

For a catalytic reactor and each candidate coke precursor, one can use the data of reactant concentration at the inlet and at each of the outlets as functions of t to test each of these correlation forms. This procedure includes the approximation that, whereas for each i these values of τ_i^* may not be the same for all times t, $a(c_p(\tau_i^*))$ is insensitive to this fluctuation in τ_i^* with t.

As it turns out all of the $q = 1$ model plots based on Table 2 yield fairly straight lines. Since for 140-hr fixed-bed runs, the values of $K_d t_{max}$ turn out to be ≤ 0.6, it is difficult to distinguish among the $q = 1$ models based solely on the straightness criterion. [These models first differ from one another at order $(K_d t)^2$.] We choose the $q = \alpha = n = 1$ model, since it shows the most systematic variation with coke content (see Figs. 11 and 13 below). Figure 10, constructed from the data in Fig. 8 (converted to molar concentrations or equivalently, since the total pressure is fixed, to molar fractions y), illustrates the excellent fit of the data to this model, yielding slope $K_d(\tau_i^*)$ and intercept $\bar{k}_i$. We have extensive data on nC_7 concentration versus time at

TABLE 2

Different Activity Functions and nC_7 Concentration-versus Time Correlations

Parameters α and n	Activity function, a	Correlation of concentration vs time	
		$q = 1$	$q = 0$
$\alpha = 1, n = 1$	$a = \exp(-K_{di} t)$	$\ln\left[\frac{\ln\left(C_{A_i}/C_{A_{i+1}}\right)}{\Delta\tau_i}\right] = \ln \bar{k}_i - K_{di} t$	$\ln(c_{A_i} - c_{A_{i+1}}) = \ln \bar{k}_i \Delta\tau_i - K_{di} t$
$\alpha = 1, n = 0$	$a = 1 - K_{di} t$	$\ln \frac{C_{A_i}}{C_{A_{i+1}}} = \bar{k}_i \Delta\tau_i (1 - K_{di} t)$	$c_{A_i} - c_{A_{i+1}} = \bar{k}_i \Delta\tau_i (1 - K_{di} t)$
$\alpha = 1, n = 2$	$a = 1/(1 + K_{di} t)$	$\left(\ln \frac{C_{A_i}}{C_{A_{i+1}}}\right)^{-1} = \frac{1}{k_i \Delta\tau_i}(1 + K_{di} t)$	$\frac{1}{C_{A_i} - C_{A_{i+1}}} = \frac{1}{k_i \Delta\tau_i}(1 + K_{di} t)$
$\alpha = 2, n = 2$	$a = 1/(1 + K_{di} t)^2$	$\left(\ln \frac{C_{A_i}}{C_{A_{i+1}}}\right)^{-1/2} = \left(\frac{1}{k_i \Delta\tau_i}\right)^{1/2}(1 + K_{di} t)$	$(c_{A_i} - c_{A_{i+1}})^{-1/2} = \left(\frac{1}{k_i \Delta\tau_i}\right)^{1/2}(1 + k_{di} t)$

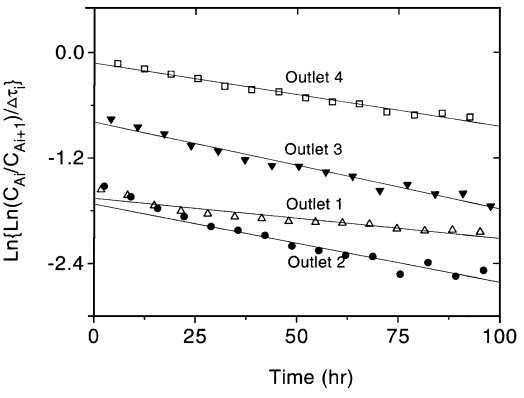

FIG. 10. Fitting of experimental data by the $\alpha = n = q = 1$ model listed in Table 2.

different operating conditions and all of them fit as well as Fig. 10.

Before using the K_d profiles along the multioutlet reactor, we examine under what conditions $\bar{k}_i$ is indeed practically independent of time. To begin, we resolve the remaining integrals in Eq. [5] using repeated applications of the mean-value theorem and different superscripts on τ for each such application.

Since $a = e^{-K_d t}$ and $c_C(t)$ are both nonnegative,

$$\int_{\tau_i}^{\tau_{i+1}} \left[\exp\left(-k_A \int_{\tau_i}^{\tau} a\,d\tau'\right)\right] a(\tau) c_c(\tau)\,d\tau$$
$$= a(\tau_i^{**}) \int_{\tau_i}^{\tau_{i+1}} \exp\{k_A a[\tau^+(\tau)](\tau - \tau_i)\} c_c(\tau)\,d\tau$$
$$= a(\tau_i^{**}) c_c(\tau_i^{***}) \int_{\tau_i}^{\tau_{i+1}} \exp\{k_A a[\tau_i^+(\tau)](\tau - \tau_i)\}\,d\tau$$
$$\approx a(\tau_i^{**}) c_c(\tau_i^{***}) \{\exp[k_A a(\tau_i^{+*})\Delta\tau_i] - 1\}/[k_A a(\tau_i^{+*})], \quad [9]$$

where the latter part of Eq. [9] uses the $\approx$ sign because it replaces $\tau_i^+(\tau)$ by a constant τ_i^{+*}. If we presume that all of the mean-value theorem τ's are approximately at the midpoint $\bar{\tau}_i$ between τ_i and τ_{i+1}, then $\bar{k}_i$ becomes

$$\bar{k}_i = k_A \left\{1 - \frac{\ln\left\{1 + \frac{k_c c_c(\bar{\tau}_i)}{k_A c_A(\tau_i)}[e^{k_A a(\bar{\tau}_i)\Delta\tau_i} - 1]\right\}}{k_A \exp[-K_d(\tau_i^*)t]\Delta\tau_i}\right\}. \quad [10]$$

Even though t appears in both the denominator and, via $a(\bar{\tau}_i)$, in the numerator of the function in Eq. [10], the dependence of $\bar{k}_i$ on t may be weak enough to almost cancel. For example, if $k_A a(\bar{\tau}_i)\Delta\tau_i \ll 1$ and $\{k_c c_c(\bar{\tau}_i)/[k_A c_A(\tau_i)]\}[e^{k_A a(\tau_i)\Delta\tau_i} - 1] \ll 1$, then expansion of both the logarithm and the exponent to leading order leads to a cancellation of the factors $a(\bar{\tau}_i) = e^{-K_d(\bar{\tau}_i)t}$ and leaves an intercept of

$$\bar{k}_i \approx k_A - k_C \frac{c_C(\bar{\tau}_i)}{c_A(\tau_i)}. \quad [11]$$

Thus if $c_c(\bar{\tau}_i, t)/c_A(\tau_i, t)$ is only weakly dependent on t and, as noted above, the mean value τ_i's are all close to the midpoints of the interval (τ_{i+1}, τ_i), then a plot of the equation for $\alpha = n = q = 1$ listed in Table 2 should lead to a straight line whose slope is $-K_d(\bar{\tau}_i)$ and whose intercept is well defined, but depends on the reactor outlet τ_i in question via $c_c(\bar{\tau}_i)/c_A(\tau_i)$ there. If, as noted, the t dependence in Eq. [10] almost cancels, plots of $\bar{k}_i$ should follow the forms in Eq. [10] or Eq. [11] with nearly t-independent coefficients.

Activity, Coke, and C5-Naphthene Profiles

Let us now test the foregoing argument against the deactivation data. Although at very high nC_7 conversions, reactions other than $iC_7 \rightarrow nC_7$ that produce nC_7 contribute, they affect r_A by less than 10% even at conversions of 95%, and so the theory above is potentially applicable even to this regime (28).

As noted, the regression in Fig. 10, constructed from the data in Fig. 8 for $(\alpha, n) = (1, 1)$, gives an excellent correlation. The deactivation "pseudoparameter" K_{di} and the $\bar{k}_i$ values derive from the slopes and intercepts of these plots. Table 3 presents the results at different experimental conditions (three flow rates × four exits). One may argue that taking the logarithm twice of almost any monotonic function will provide a plot that looks linear. But, as noted, plots for other $q = 1$ models are also fairly linear and provide parameter values that are in the same ball park. Moreover, as Fig. 11 shows, the pseudoparameter K_{di} correlates very well with coke buildup and with the concentration profile of one and only one set of the reaction participants, the suspected coke precursors, as we discuss below.

Finally, Eq. [10] or [11], using the values $y_{iC_7}(\bar{\tau}_i) \approx [y_{iC_7}(\tau_i) + y_{iC_7}(\tau_{i+1})]/2$ and $y_{nC_7}(\tau_i)$, explains the variation

TABLE 3

K_d, $\bar{k}_i$, and iC_7 Concentrations (Mole Fractions) Obtained at Different Space Times ($T = 750$ K, $P = 517$ kPa, $H_2/nC_7 = 3$)

	Space time (g cat. min/g oil)											
	30	15	10	7.5	6	4.29	3.33	2.31	1.05	0.55	0.50	0.45
$K_d(\tau) \times 10^3 (hr^{-1})$	0.41	0.98	1.89	2.0	2.50	2.75	2.69	2.54	2.65	2.24	1.80	1.45
$\bar{k}_i (hr^{-1})$	4.26	6.36	7.96	9.51	10.5	10.8	12.7	14.2	17.3	18.2	20.5	18.2
$\bar{y}_{iC_7}$	0.21	0.34	0.39	0.38	0.34	0.33	0.28	0.22	0.12	0.08	0.08	0.05
y_{nC_7}	0.06	0.15	0.22	0.31	0.38	0.46	0.56	0.65	0.82	0.87	0.87	0.90

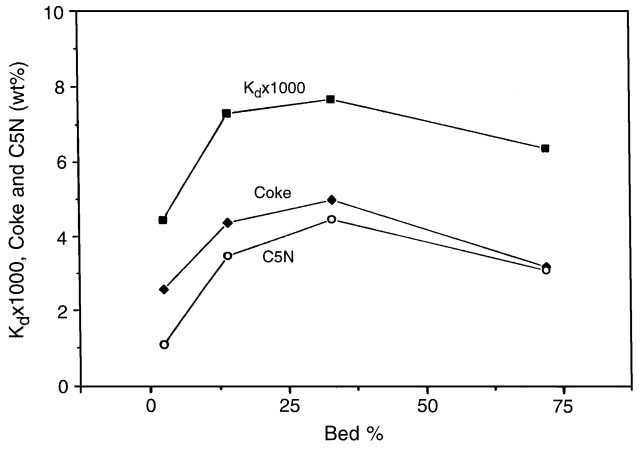

FIG. 11. Profiles of C5 naphthenes, coke, and K_d along the catalyst bed at $t = 170$ hrs.

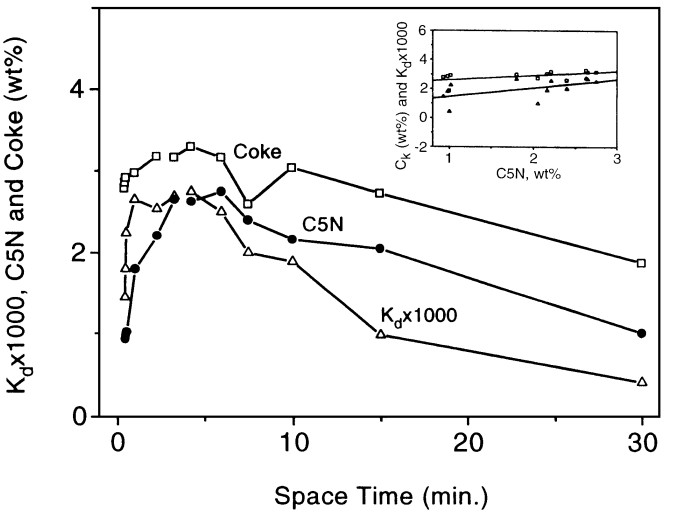

FIG. 13. C5 naphthenes, coke, and K_d as a function of space time τ for different on-stream times (170, 224, 240 hr). Inset: parametric plot.

of $\bar{k}_i$ with τ quite well, as the solid circles (y_{iC_7} and y_{nC_7} data at $t = 40$ hr) in Fig. 12 illustrate. What we need to do next is to test if $\bar{k}_i$ is indeed a weak function of t.

Figure 12 actually plots $\bar{k}_i$ versus $c_c(\bar{\tau}_i, t)/c_A(\tau_i, t)$ for t evaluated at three times, 40, 70, and 100 hr, all after the initial transient. The lines are regression results based on Eqs. [10] and [11], with the former for regression purposes being rewritten as

$$\bar{k}_i = k_A \left[1 - \beta \ln \left(1 + \gamma \frac{c_c(\bar{\tau}_i)}{c_A(\tau_i)} \right) \right], \qquad [12]$$

where $\gamma = [k_A \exp(-K_d t)\Delta\tau]^{-1}$. With this equation, a single curve fits the data at all three times quite well. This illustrates that the curve is essentially time independent and thus $\bar{k}_i$ is primarily a function of τ through the concentration ratio $\bar{c}_c/c_A$. Table 4 further illustrates this point by providing the best-fitting parameters for each of the data sets individually and combined. Note that k_A and β are practically time-independent and γ's fluctuation is well within its standard deviation. (This latter value is large because the form of Eq. [12] has the property that small changes in the data yield large changes in γ.) As Fig. 12 and Table 4 show, the linear fit based on Eq. [11], not surprisingly, is only qualitative. Finally, we stress that as long as one considers data for which the $\Delta\tau$ between adjacent τ_i values is small, the approximation of the mean-value theorem positions by the midpoint between τ_i and τ_{i+1} is probably reasonable. That $\Delta\tau$ is larger for the large τ (large conversion) experiments probably accounts for the larger scatter of points at the same τ_i value from each other (but not from the solid curve) at the right of Fig. 12. As noted earlier, our treatment may eventually break down at large τ.

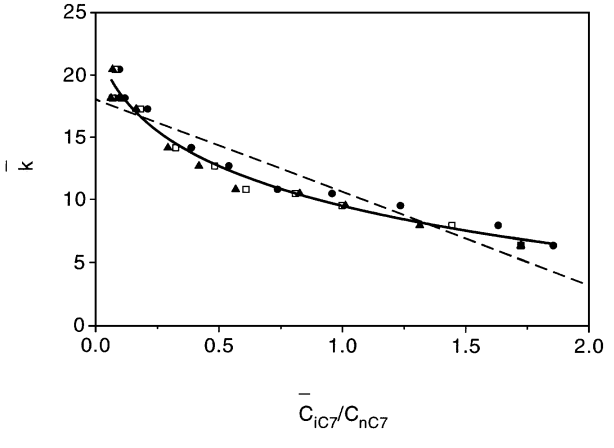

FIG. 12. $\bar{k}_i$ as a function of $c_c(\bar{\tau}_i, t)/c_A(\tau_i, t)$ for $t = 40$ (●), 70 (□), and 100 (△) hr. - - -, Eq. [11]; —, Eq. [12].

Since our reactor has only four outlets, each circa ~170-hr run provides only four data points for the coke, C5N, and K_d profiles. To assemble more data, we also plot the collected coke, C5N, and K_d data versus the 12 space velocities corresponding to three separate runs in Fig. 13. All three runs had the same temperature, pressure, and H_2/nC_7 mole ratio, but different on-oil times (240, 224, and 170 hr); hence the data in Fig. 13 are not as smooth as those of Fig. 11. The three profiles only appear to cross due to the choice of scale. This figure shows the profiles of deposited coke[3], the corresponding time-averaged C5N concentrations and the K_d values. Remarkably, all three profiles are extremely similar. That K_d and C_k track each other closely as to almost be

[3] Note that the TPO value for the coke concentrations in the ith reactor section is an average value for the section of the bed between outlets i and $i+1$. Assuming that the coke concentration is a continuous function of bed position τ, there is at least one position in section i where the coke concentration takes on that value. Just as in the mean-value theorem arguments above, we approximate these positions by the section midpoints.

TABLE 4

Values of Best-Fitted Parameters for Eqs. [11] and [12]

Time t (hr)	Equation [12]			Equation [11]	
	k_A	β	γ	k_A	k_C
40	21.76 ± 1.51	0.26 ± 0.073	6.98 ± 5.66	18.25 ± 0.75	7.01 ± 0.80
70	22.10 ± 1.60	0.24 ± 0.062	10.06 ± 8.08	18.06 ± 0.81	7.73 ± 0.98
100	21.97 ± 1.64	0.23 ± 0.06	11.34 ± 9.02	17.92 ± 0.82	7.82 ± 1.03
Combined	22.00 ± 0.95	0.24 ± 0.04	10.10 ± 4.88	18.01 ± 0.44	7.40 ± 0.52

multiples of one another, i.e., $K_d \approx \xi(t)C_k(t)$, agrees with Froment's group's (24, 26) findings, as we anticipated. That is, $a = e^{-K_d t} \approx e^{-\alpha C_k}$, where $\alpha = \xi(t)t$, t being the time of the run. Note that α being independent of t is equivalent to C_k being proportional to t.

All three profiles in Fig. 13 exhibit a maximum at a space time of about 5 min under these experimental conditions, which indicates that the coke derives from a reforming intermediate. That is, since unlike the flowing gas the catalyst is stationary and builds up coke in place, the fact that coke concentration C_k goes through a maximum in τ suggests that its rate of production and hence its precursor's concentration do the same. Clearly, it would be preferable to plot the profile of the rate dC/dt rather than of C_k. Unfortunately, TPO analysis of the fixed-bed data do not provide such data and we defer such an analysis to the next section (see Fig. 17). On the other hand, if the precursor concentration is time invariant, then dC_k/dt will be as well, and $C_k(t)$ is just proportional to dC_k/dt. The fact (Fig. 9) that the C5N concentrations are fairly flat after the initial transients and the tracking of the curves in Figs. 11 and 13 are consistent with C5N being the major coke precursors and with this interpretation.

DETAILED VIBRATIONAL MICROBALANCE STUDIES

Up to this point, we have assembled a battery of evidence that, in aggregate, suggests C5N as the major coke precursor in *n*-heptane reforming. This finding is consistent with that of Querini and Fung (13) whose experiments covered a relatively narrow range of conditions; however, all these data are integral in nature and thus leave some room for doubt. Below we employ the new vibrational microbalance with its *in situ* coke measuring and simultaneous reactor gas-phase monitoring capabilities to provide our final, most direct and quantitative evidence.

Figures 14 and 15 show the effects of space velocity on coke and C5N, both as functions of on-stream time over the $Pt{-}Re/Al_2O_3$ catalyst. Here the faster rate of coke buildup at low space velocities, just as the fall in activity in Fig. 8, is associated with the higher C5N concentrations.

To further quantitatively determine which of the hydrocarbon groups is the major source of coke and also to test the conjectures/conclusions in the literature, we perform experiments to compare the coking rates of different hydrocarbon (HC) feeds in the vibrational microbalance at 207 kPa, 750 K, and $H_2/HC = 3.0$ over the $Pt{-}Re/Al_2O_3$ catalyst. Figure 16 shows the coking rates of the following feeds:

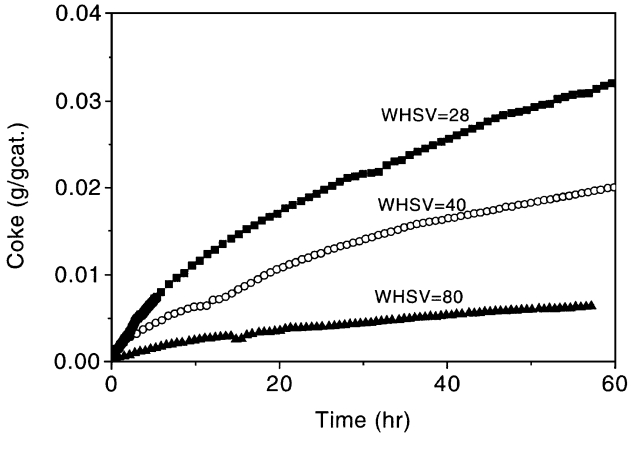

FIG. 14. Coke versus time on-stream at different WHSVs; data obtained from vibrational microbalance at 207 kPa.

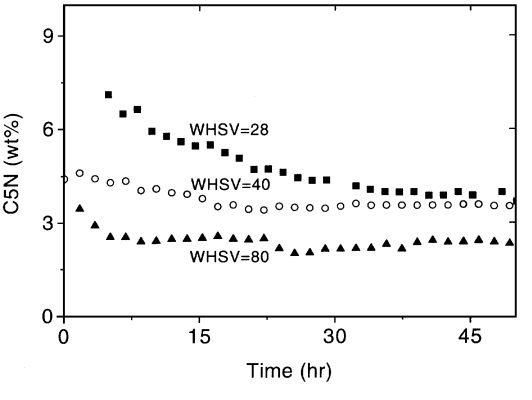

FIG. 15. Total concentration of five-carbon ringed naphthenes versus time on-stream at different WHSVs; data obtained from vibrational microbalance at 207 kPa.

toluene, nC_7, 96% toluene + 4% ECP, 96% toluene + 4% MCP, 50% toluene + 50% MCP, and pure MCP and ECP. MCP and ECP are two of the C5Ns that hexane and heptane reforming generates.

Figure 16 shows that the pure MCP and pure ECP feeds produce significant amounts of coke and, in fact, much more than pure nC_7 or toluene feeds. This indicates that C5Ns are potent coke precursors in paraffin reforming and, in fact, are much more potent than the feed or product. It is consistent with the multioutlet fixed-bed reactor results and with the conjecture of Zhorov and Panchenkov (7).

Van Trimpont *et al*. (26) proposed that the intercondensation between toluene and C_7 cyclopentadienes is responsible for most of the coke in nC_7 reforming. To test this hypothesis, we compare the coking rate of a 50% MCP + 50% toluene mixture feed with the coking rate of pure MCP. Presumably, Van Trimpont *et al*. would expect the coking rate of a 50/50 MCP/toluene feed to be faster than that of pure MCP. As it turns out, though, Fig. 16 shows the opposite is true; it is thus difficult to conclude that these data are consistent with the proposition that the intercondensation between toluene and C_7 cyclopentadienes is the primary source of coke. Figure 17 shows that the initial coking rate is in fact linear in the partial pressure of MCP.

At this point, it is natural to conjecture that C5Ns actually account for most of the *n*-heptane reforming coke. Under the conditions employed, the nC_7 feed produces a total of ~4 wt% C5N at the exit of the microbalance. Also, the coking rate of toluene in Fig. 16 is much lower than that of nC_7, MCP, or ECP. So, it is easy to test our conjecture by feeding the 4% C5N + 96% toluene into the microbalance and comparing the resulting coking rate with that of pure nC_7. As Fig. 16 shows, these two are quite similar with either MCP or ECP as the model compound of C5N. Finally, note that the coking rates of MCP and ECP are almost indistinguishable from each other. This indicates that at least

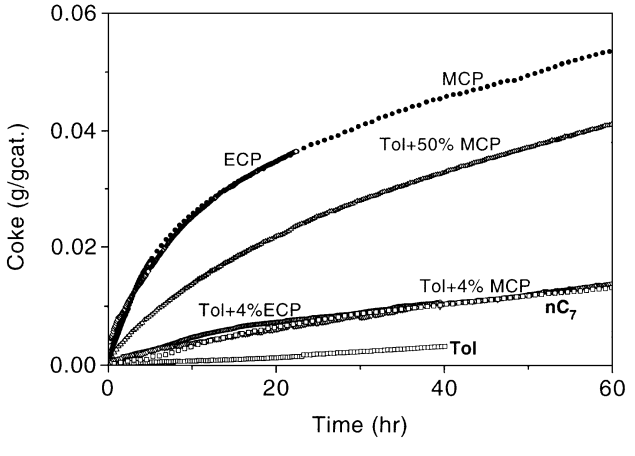

FIG. 16. Coke versus time on-stream for different hydrocarbon feeds; data obtained from vibrational microbalance at 207 kPa.

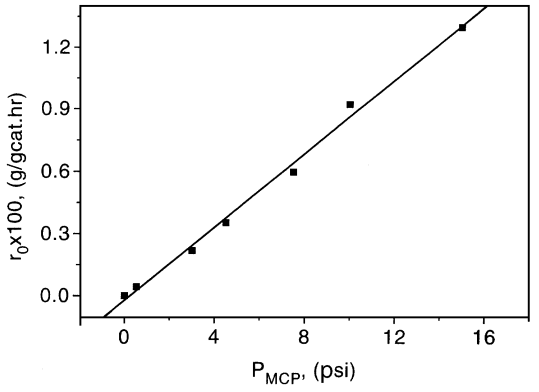

FIG. 17. First-order dependence of initial coking rate on methylcyclopentane partial pressure.

two and maybe all different C5Ns have similar coking rates. Hence, it is reasonable to use the readily available and relatively inexpensive MCP as the model compound for C5N to study coking kinetics.

CONCLUSIONS AND OUTLOOK

The coincidence of the C5N concentration trends and coking trends with pressure, temperature, and space velocity; the tracking of C5N, coke, and deactivation profiles in the fixed-bed reactor; and the differential microbalance coking studies all point to the same conclusion: The catalyst coke in paraffin reforming derives mainly from the C5N intermediates; the more C5 naphthenes produced, the more coke forms and the faster the rate of deactivation. The microbalance studies also show that toluene contributes little to the coke formation and MCP is an adequate model compound of C5Ns for detailed coking kinetics studies as well as for exploratory studies aimed at developing more robust catalysts (e.g., C5Ns can be used in accelerated aging tests). These results clarify some of the controversies regarding the coking mechanisms reported in the literature. Moreover, since the C5 naphthene concentration is not uniform along the catalyst bed, neither are the coke content and the rate of catalyst deactivation. This explains why the coking and deactivation rates correlate with the space velocity and hence finally why the coke formation in the fixed bed is not uniform.

To carry out this work, we have developed a new microbalance reactor system that simultaneously provides accurate measurements of coking kinetics and reliable reaction kinetic data. This is because the flow-through design of the vibrational microbalance eliminates the feed gas bypassing problem encountered in traditional thermogravimetric microbalances. The flow-through capability and the high sensitivity and stability of the vibrational microbalance make it an ideal general tool for research not only in catalyst coking/decoking kinetics studies under realistic

conditions but also in absorption/adsorption and desorption studies; gas–solid reactions involving mass gain/loss; solvent recovery/destruction analysis; desiccant characterization; gas density and catalyst pore volume measurements; and catalyst characterization and regeneration.

Modeling industrial catalytic reforming processes and predicting the coke profile require a knowledge of the kinetics of both the main reaction and the side coking reactions that cause catalyst deactivation. The coke profile is a crucial input to the simulation and control of the catalyst regeneration process. An uneven coke distribution along the catalyst bed can lead to sharp temperature spikes that can severely damage the catalyst. Unfortunately, it is almost impossible to do on-line coking rate measurement for a commercial reformer; on the other hand, it is easier to do on-line gas product analysis of a commercial reformer. Thus, the identification of C5N as the primary coke precursor holds out the possibility of accurate inference of the state of coking and of the coke profile of an operating reformer from the gas-phase monitoring of the C5N concentration along the bed.

Two obvious questions remain: (1) To predict the amount of coke being formed and the resulting catalyst coke profile from C5N concentration data requires a coking kinetics model. Can a satisfactory one be developed? (2) Can a simple model for the reforming reactions be developed that includes a C5N lump and thus that accurately predicts the C5N profile? We shall attempt to answer these questions in future papers.

APPENDIX: NOMENCLATURE

a	activity function
c_p	concentration of coke precursor
c_A	reactant (*n*-heptane) concentration
C_k	total amount of coke deposited on the catalyst, g coke/g catalyst
C5N	five-carbon atom ring naphthenes
f	catalyst's unused fouling capacity
k	reaction rate constant
k_i	defined in Eq. [5]
K_d	deactivation parameter, Eq. [3]
m	total oscillating mass
n	deactivation order, Eq. [3]
P	total pressure, kPa
q	order of main reaction, Eq. [3]
P_{H_2}	partial pressure of H_2, kPa
r_A	reaction rate of component A
r_0	reaction rate of component A at time zero
t	on-stream time
T	temperature, K
V	volume, cm^3
W	weight of the catalyst, g

Greek Letters

α	number of active sites involved in the rate-controlling step
β	$[k_A \exp(-K_d t)\Delta\tau]^{-1}$
τ	space time, g cat. min/g oil
κ	spring constant
γ	$k_c[\exp(k_c a \Delta\tau_i - 1)]/k_A$
ν	frequency

REFERENCES

1. Butt, J., and Petersen, E. E., "Activation, Deactivation and Poisoning of Catalyst." Academic Press, London, 1988.
2. Franck, J. P., and Martino, G., *in* "Deactivation and Poisoning of Catalysts," p. 205. Marcel Dekker, New York, 1985.
3. Beeckman, J. W., and Froment, G. F., *Ind. Eng. Chem. Fundam.* **18**, 245 (1979).
4. Figoli, N. S., Beltraminal, J. N., Martenelli, E. E., and Parera, J. M., *J. Chem. Technol. Biotechnol.* **32**, 445 (1982).
5. Mieville, R. L., *in* "Catalyst Deactivation" (C. H. Bartholomew and J. B. Butt, Eds.). Elsevier, Amsterdam, 1991.
6. Voorhies, A., Jr., *Ind. Eng. Chem.* **37**, 318 (1945).
7. Zhorov, Yu. M., and Panchenkov, G. M., *Kinet. Katal.* **21**(3), 776 (1980).
8. Myers, G. A., Lang, W. H., and Weisz, P. B., *Ind. Eng. Chem.* **53**, 299 (1961).
9. Cooper, B. J., and Trim, D. L., *in* "Catalyst Deactivation" (B. Delmon and G. F. Froment, Eds.), p. 63. Elsevier, Amsterdam, 1980.
10. Clem, K. R., Ph.D. Dissertation, Louisiana State University, 1977.
11. Sinfelt, J. H., and Rohrer, J. C., *J. Chem. Eng. Data* **8**, 109 (1963).
12. Parera, J. M., Verderone, R. A., and Querini, C. A., *in* "Catalyst Deactivation" (B. Delmon and G. F. Froment, Eds.), p. 135. Elsevier, Amsterdam, 1987.
13. Querini, C. A., and Fung, S. C., *J. Catal.* **141**, 389 (1993).
14. Marin, G. B., and Froment, G. F., *Chem. Eng. Sci.* **37**(3), 759 (1982).
15. Lin, C., Park, S. W., and Hatcher, W. J., Jr., *Ind. Eng. Chem. Process Des. Dev.* **22**(4), 609 (1983).
16. Dean, J. W., and Dadyburjor, D. B., *Ind. Eng. Chem. Res.* **27**(10), 1754 (1988).
17. Mieville, R. L., *J. Catal.* **100**, 482 (1986).
18. Biswas, J., Gray, P. G., and Do, D. D., *Appl. Catal.* **32**, 249 (1987).
19. Fung, S. C., Querini, C. A., Ke Liu, Rumschitzki, D. S., and Ho, T. C., *in* "Catalyst Deactivation 1994" (B. Delmon and G. F. Froment, Eds.), Studies in Surface Science and Catalysis, Vol. 88, pp. 305–312. Elsevier, Amsterdam, 1994.
20. Patashnick, H., Rupprecht, G., and Wang, J. C. F., *Prepr. ACS Div. Petr. Chem.* **25**, 188 (1980).
21. Hershkowitz, F., Kleshgi, H. S., and Madiara, P. D., *Prepr. ACS Div. Petr. Chem.* **38**, 619 (1993).
22. Fung, S. C., and Querini, C. A., *J. Catal.* **138**, 240 (1992).
23. Fung, S. C., Querini, C. A., and McCoy, C. J., *in* "Catalyst Deactivation" (C. Bartholomew and J. Butt, Eds.), p. 135. Elsevier, Amsterdam, 1991.
24. Szepe, S., and Levenspiel, O., *in* "Proceedings of Fourth European Symposium." Pergamon, London, 1971.
25. Van Trimpont, P. A., Marin, G. B., and Froment, G. F., *Appl. Catal.* **24**, 53 (1986).
26. Van Trimpont, P. A., Marin, G. B., and Froment, G. F., *Ind. Eng. Chem. Res.* **27**(1), 51 (1988).
27. Ramage, M. P., Graziani, K. R., Schipper, P. H., Krambeck, F. J., and Choi, B. C., *Adv. Chem. Eng.* **13**, 193 (1987).
28. Liu, K., Fung, S. C., Ho, T. C., and Rumschitzki, D. S., in preparation (1997).